Mesoscopic Behavior of Single-Carrier Avalanche in Narrow-Bandgap Semiconductors

Shuning Liu, Runzhang Xie, Qianlong Kang, Haonan Ge, Min Luo, Anna Liu, Hao Xie, Lu Chen, Xiwen Liu, *Member, IEEE*, Qing Li, and Weida Hu, *Fellow, IEEE*

***Abstract*— The mesoscopic stochasticity of single-carrier avalanche is the dominant factor governing macroscopic noise in narrow-bandgap avalanche photodiodes (APDs). In mercury cadmium telluride (HgCdTe) devices, this randomness induces local electric field fluctuations that trigger gain-limiting band-to-band tunneling (BBT) noise. Traditional macroscopic models inherently average out these statistical fluctuations, while purely microscopic simulations are often computationally prohibitive for iterative design. To bridge this gap, this work presents a micro–mesoscopic coupled Monte Carlo framework developed to analyze avalanche chain dynamics at the critical mesoscopic scale. The analysis reveals that the avalanche statistics are governed by a coupled, 2-D parameter space defined by the spatial standard deviation (σ) and the mean free path (ℓ). We demonstrate that the macroscopic signal-to-noise ratio (SNR) is determined by a complex competition among multiple noise mechanisms, involving Auger, BBT, phonon, and excess noise mechanisms within this parameter space. Guided by this analysis, an acceleration meso-lattice (AML) structure is proposed to actively engineer the mesoscopic state near a precisely optimal operating point. By regulating carrier dynamics to suppress stochastic fluctuations at their origin, the AML structure suppresses the physical conditions for BBT noise and achieves significant SNR enhancement. This research shifts the design paradigm from macroscopic geometric optimization to direct mesoscopic dynamics regulation, offering a new physical pathway to transcend fundamental device limits.**

***Index Terms*— Avalanche photodiodes (APDs), mercury cadmium telluride (HgCdTe), mesoscopic dynamics, Monte Carlo methods.**

I. Introduction

MERCURY–CADMIUM–TELLURIDE (HgCdTe) avalanche photodiodes (APDs) are a cornerstone of high-sensitivity infrared detection, widely applied in night vision, LiDAR, infrared communication, and space astronomy [1], [2], [3], [4]. Due to their tunable bandgap, HgCdTe APDs maintain extremely high quantum efficiency across a broad spectrum, from near- to far-infrared [5], [6]. However, achieving high-gain amplification necessitates operation under high electric fields, which concurrently induces severe band-to-band tunneling (BBT) [7], [8]. When the field strength is excessive, valence band electrons can tunnel directly into the conduction band, creating dark current independent of the avalanche multiplication. This current is not only highly dependent on the device's electric field distribution but also exhibits strong statistical randomness, becoming a primary source of performance degradation. This conflict between gain and noise at high fields constitutes the central, longstanding challenge in HgCdTe APD design [9].

Traditional device modeling, such as McIntyre's classical history-independent model, typically relies on assumptions of a local electric field and average carrier energy [10], [11]. While efficient for describing quasi-equilibrium transport, these models often fail to provide accurate predictions when faced with the nonlocal impact ionization (ii) and quantum tunneling mechanisms inherent in the avalanche process [12]. Conversely, while full-band Monte Carlo (FBMC) methods can fully reproduce the entire process of carrier energy accumulation, scattering, and ionization with high physical fidelity, their prohibitive computational cost makes them impractical for the frequent structural iterations required in device design [13], [14]. Balancing physical rigor with computational efficiency remains a critical bottleneck in APD research.

To address this, we propose a micro–mesoscopic coupled Monte Carlo framework. This framework bridges the gap between physical accuracy and computational efficiency by precisely calculating individual carrier energy evolution tra-

Received 14 December 2025; revised 30 January 2026; accepted 11 February 2026. Date of publication 2 March 2026; date of current version 26 March 2026. This work was supported in part by the National Natural Science Foundation of China under Grant 62327812, Grant 62522414, Grant 62205360, and Grant 62305359; in part by the National Key Research and Development Programme of China under Grant 2025YFF0520500; and in part by Shanghai Youth Elite Sailing Program under Grant 23YF1455200. The review of this article was arranged by Editor J. D. Phillips. *(Corresponding authors: Runzhang Xie; Weida Hu.)*

Shuning Liu is with the State Key Laboratory of Infrared Physics, Shanghai Institute of Technical Physics, Chinese Academy of Sciences, Shanghai 200083, China, and also with the Thrust of Microelectronics, Hong Kong University of Science and Technology (Guangzhou), Guangzhou 511453, China.

Runzhang Xie, Qianlong Kang, Haonan Ge, Min Luo, Anna Liu, Hao Xie, Lu Chen, and Weida Hu are with the State Key Laboratory of Infrared Physics, Shanghai Institute of Technical Physics, Chinese Academy of Sciences, Shanghai 200083, China (e-mail: xierunzhang@mail.sitp.ac.cn; wdhu@mail.sitp.ac.cn).

Xiwen Liu is with the Thrust of Microelectronics, Hong Kong University of Science and Technology (Guangzhou), Guangzhou 511453, China.

Qing Li is with Hangzhou Institute for Advanced Study, Hangzhou 310024, China.

Digital Object Identifier 10.1109/TED.2026.3666174

1557-9646 © 2026 IEEE. All rights reserved, including rights for text and data mining, and training of artificial intelligence and similar technologies. Personal use is permitted, but republication/redistribution requires IEEE permission.
See https://www.ieee.org/publications/rights/index.html for more information.
Authorized licensed use limited to: Shanghai Institute of Technical Physics CAS. Downloaded on April 01,2026 at 02:47:06 UTC from IEEE Xplore. Restrictions apply.

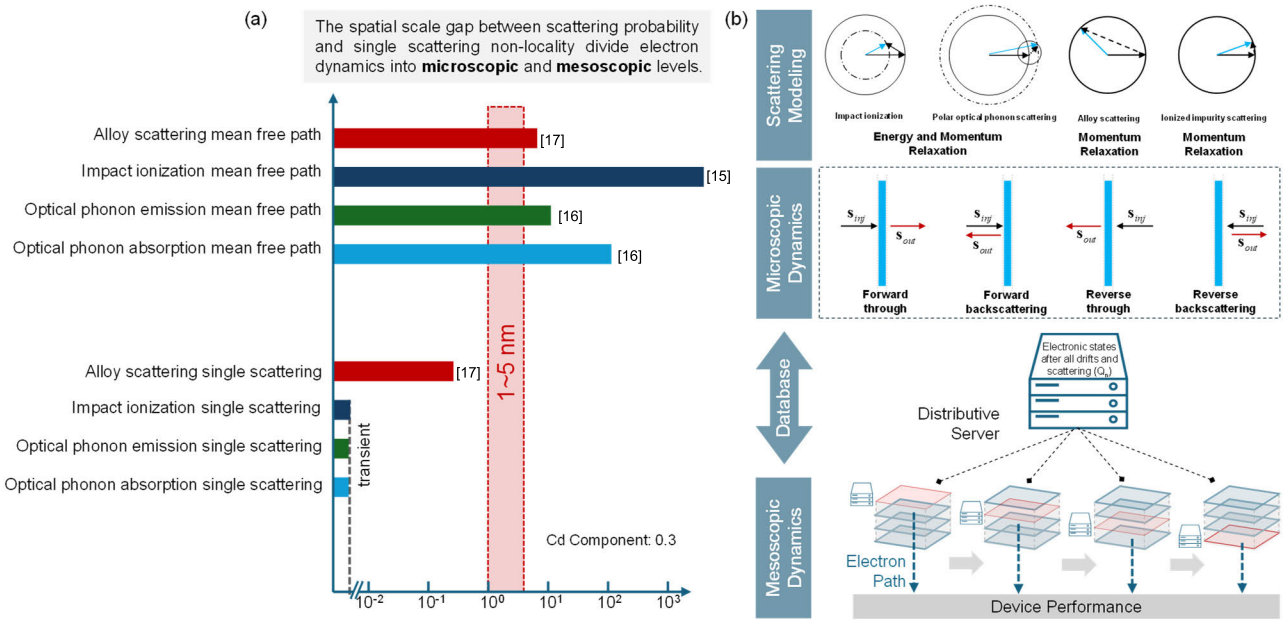


Fig. 1. Micro–mesoscopic coupled Monte Carlo framework. The framework is designed to bridge the physical scale gap between microscopic scattering physics and macroscopic device performance. (a) Spatial scale gap between the mean free path of various scattering events and the nonlocal. (b) Microscopic dynamics kernel (top) rigorously simulates quantum-mechanical scattering mechanisms (e.g., impact ionization [15], POP [16], alloy scattering [17]) from quantum mechanics. These computationally intensive results are precompiled into a statistical database. The mesoscopic dynamics kernel (center) efficiently queries this database to reconstruct carrier trajectories. This architecture enables the analysis of mesoscopic statistical behavior and links it directly to macroscopic device performance (bottom). The database stores precalculated electron states from drift and scattering.

jectories at the microscale and using a statistical database for large-scale acceleration at the mesoscale. Leveraging this framework, we design an acceleration meso-lattice (AML) structure. This structure, through engineered band-gradient and doping profiles at the mesoscopic scale, transforms the avalanche's spatial distribution from random diffusion into a highly deterministic, localized process, thereby physically suppressing BBT-induced noise.

II. Simulation Framework

The core of our framework is the decoupling of carrier dynamics into two interconnected scales: microscopic and mesoscopic (Fig. 1). This constructs a simulation system that balances physical rigor with computational efficiency. The left panel of Fig. 1, which illustrates the spatial scale gap between the mean free path of various scattering events and the transient, nonlocal nature of single scattering, explicitly motivates this decoupled approach [18], [19].

At the foundational microscopic scale (Fig. 1(b), top), we return to first principles, using a quantum-mechanics based Monte Carlo method built from quantum mechanics to simulate all the key scattering events that determine a carrier's nonlocal behavior. Our microscopic kernel precisely simulates every step of this process, including impact ionization [15], polar optical phonon (POP) scattering, [16], and alloy scattering [17]. By simulating these processes, we accurately track the complete evolutionary history of an electron in energy-momentum space, fully capturing the nonlocal characteristics inherent to avalanche multiplication.

The technical challenge of this framework lies in the computational cost of the microscopic kernel. Accurately simulating the full spectrum of quantum-mechanical scattering events—such as POP scattering, alloy scattering, and nonlocal impact ionization—from first principles is an endeavor that typically requires massive supercomputing resources, rendering it impractical for iterative device design [20]. A key innovation of our framework is the decoupling of this computationally intensive physics calculation from the device-level simulation. We leverage high-performance computing once to precalculate and exhaustively map the results of these microscale interactions across a vast parameter space of initial conditions (e.g., fields, energies, angles).

These precalculated results are systematically compiled into what we term the quantum transport core database (Fig. 1(b), center), which serves as the precompiled physics library for our framework. To implement the look-up table method mathematically, we define the discrete incident electron state as a vector $\mathbf{s}_{inj} = (i_{vx}, i_{vz}, i_{Pz}, \delta)$, where i_{vx}, i_{vz} and i_{Pz} denote the indices for the velocity components and position, respectively, and δ represents the discrete motion direction index. The database contains N_s samples for each state. v_{idx} spans $0 - N_v$ (3 eV), and θ_{idx} defines N_θ angular segments.

The innovative architecture of the framework is in how the mesoscopic-scale kernel operates: it no longer performs real-time, complex Monte Carlo calculations. Instead, it reconstructs trajectories via a stochastic iterative mapping. For each incident state $\mathbf{s}_{inj}$, the impact ionization probability $p_{ii} = (\mathbf{s}_{inj})$ is retrieved. We use random numbers r_1 and r_2 to determine the occurrence of ionization and to select the specific output

Authorized licensed use limited to: Shanghai Institute of Technical Physics CAS. Downloaded on April 01,2026 at 02:47:06 UTC from IEEE Xplore. Restrictions apply.

sample index from the database, respectively. $r_1 < P_{ii}(S_{inj})$ triggers ionization; r_2 selects S_{out} based on the cumulative distribution function.

Boundary conditions are handled such that reflection maps the index of z to $i_{Pz} - 1$, while transmission maps to $i_{Pz} + 1$. Consequently, a single transport step is described by the state transfer function

$$\mathbf{s}_{out} = f\left(\mathbf{s}_{inj}, \mathbf{r}\right) \tag{1}$$

where $\mathbf{r} = (r_1, r_2)$. This formalism generalizes to the avalanche regime by extending f to matrix arguments for n electrons. Upon impact ionization, the function branches to generate dual output states (hot and cold carriers)

$$[\mathbf{s}_{hot}, \mathbf{s}_{cold}]^T = f\left(\mathbf{s}_{inj}, \mathbf{r}\right). \tag{2}$$

"Hot" denotes high-energy primaries, while "cold" represents band-edge secondaries. This allows the complex avalanche dynamics to be expressed as a concise iterative recursion $f_n(\mathbf{s}_{inj}, \mathbf{r}) = f^n(\mathbf{s}_{inj}, \mathbf{r})$. This coupled micro–mesoscopic method significantly accelerates the simulation by orders of magnitude. More importantly, it is this framework that provides profound insight and control over the device's internal mesoscopic states–specifically, yielding the statistical distribution of impact ionization events, characterized by its mean (ℓ) and standard deviation (σ), which forms the direct physical basis for our meso-lattice (ML) structure [21]. Microscopic models bulk properties, and mesoscopic handles ideal contacts.

III. Results and Discussion

The physical accuracy of our micro–mesoscopic coupled Monte Carlo framework was first validated through an analysis of a conventional HgCdTe p-i-n APD structure [see Fig. 2(a)] [22], [23]. The simulation results show high consistency with experimental data [see Fig. 2(b)] for both (c) multiplication gain (M) versus reverse bias and (d) excess noise factor (ENF) versus gain [see Fig. 2(c) and (d)]. A subsequent decomposition of the simulated dark current components [see Fig. 2(f)] into BBT, trap-assisted tunneling (TAT) and Shockley–Read–Hall (SRH) recombination, and Avalanche current reveals that in the high-gain region, BBT current rapidly becomes the overwhelming noise source, fundamentally constraining the device's signal-to-noise ratio (SNR) [7], [24], [25].

The predominance of BBT noise stems from the inherent physical limitations of p-i-n design. As shown in the simulated electric field profiles [see Fig. 2(e)], achieving avalanche multiplication necessitates a high-intensity electric field peak (E_{peak}) with an extremely sharp spatial gradient (dE/dx) at the p–n-junction. Our analysis reveals that the direct cause of BBT is not merely the high static field itself, but rather the local electric field fluctuations induced by the inherent stochastic nature of the avalanche chain. A highly stochastic avalanche, spatially diffused in its ionization events [visualized later in Fig. 3(c)], leads to nonuniform instantaneous carrier density distributions, superimposing transient electric field spikes onto the static field background, which dynamically triggers BBT [26]. This insight forms the core argument of our work: the root of the problem is the uncontrolled, stochastic avalanche dynamics. This necessitates a new design philosophy, shifting the focus from optimizing macroscopic geometry to actively regulating carrier dynamics at the mesoscopic scale—a concept we term mesoscopic dynamics regulation.

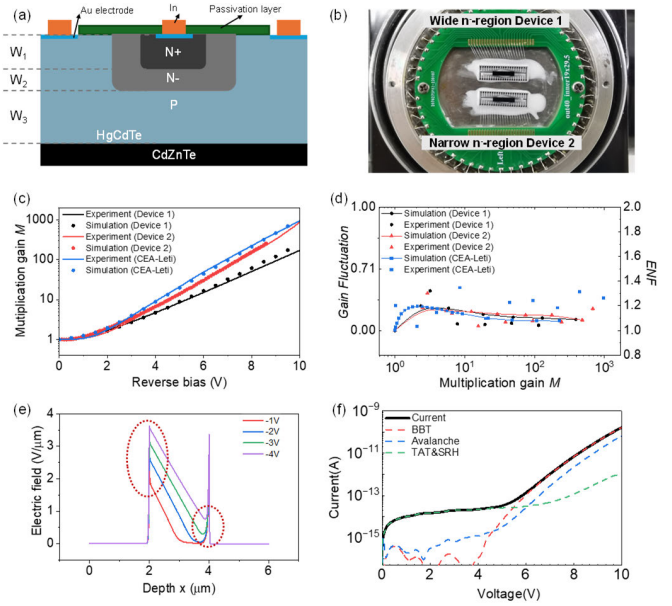


Fig. 2. Validation of the micro–mesoscopic framework and noise mechanism analysis of conventional HgCdTe p-i-n APDs. (a) Schematic of the p-i-n device structure. (b) Photographs of wide n-region Device 1 and narrow n-region Device 2. (c) and (d) Validation of the framework, showing high consistency between simulation results (lines) and experimental data (points) for (c) multiplication gain (M) versus reverse bias and (d) gain fluctuation and ENF versus gain. (e) Simulated electric field profiles at various biases, showing the sharp peaks at the p–n and n^-–n-junction. These peaks are a prerequisite for gain but also one of the root causes of tunneling. (f) Decomposition of simulated dark current components, including BBT, TAT and SRH recombination, and Avalanche current. The analysis identifies BBT as the dominant noise source in the high-gain region (≥5 V), fundamentally limiting device performance.

To realize this mesoscopic dynamics regulation, we must first establish a set of physical metrics. As illustrated in the conceptual diagram [see Fig. 3(a)], our framework connects microprocesses to the device level via these mesoscopic statistics. This study introduces a 2-D mesoscopic parameter space defined by the spatial separation parameter (σ) and the temporal coherence parameter (ℓ). These two parameters are the fundamental descriptors of the avalanche's mesoscopic state. The spatial separation parameter, σ, physically describes the spatial concentration of the ionization statistical distribution, quantifying the determinism (randomness) of the ionization event's location. Mathematically, it is the statistical standard deviation of the ionization position, $\sigma = (\langle x_{ii}^2 \rangle - \langle x_{ii} \rangle^2)^{1/2}$. A large σ corresponds to the stochastic, diffuse avalanche in p-i-n structures [see Fig. 3(c)], while a small σ implies a highly localized, deterministic event. The temporal coherence parameter, ℓ, physically describes the average transit distance required for a carrier to gain sufficient energy (e.g., the ionization threshold E_{th}) to trigger the *next* impact ionization. Mathematically, it is the average distance between adjacent ionizations, $\ell = \langle \Delta x_{ii} \rangle$, and char-

Authorized licensed use limited to: Shanghai Institute of Technical Physics CAS. Downloaded on April 01,2026 at 02:47:06 UTC from IEEE Xplore. Restrictions apply.

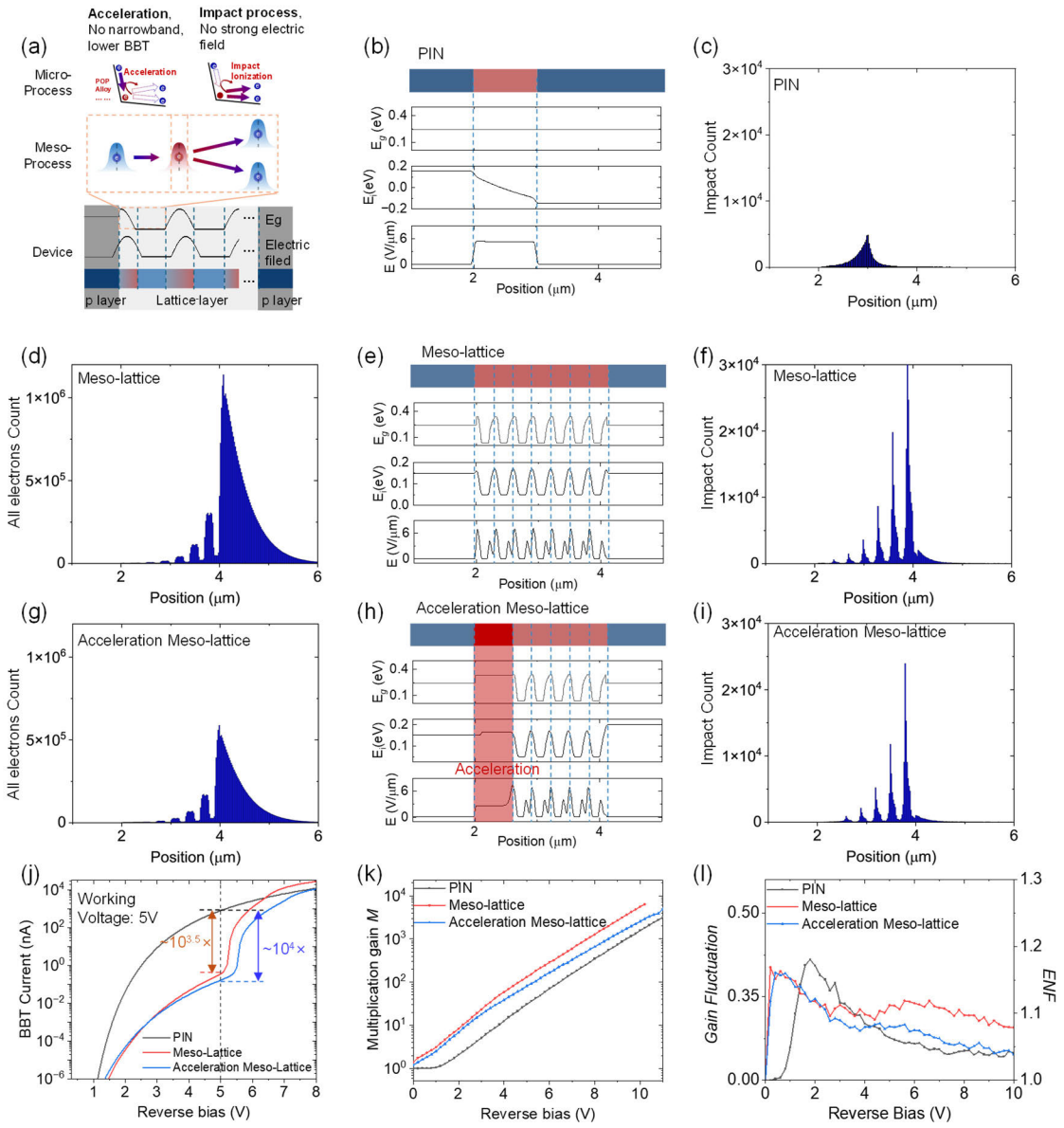


Fig. 3. Simulated device performance comparison between p-i-n, ML, and AML models. (a) Conceptual model illustrating the relationship between microprocesses (e.g., acceleration, impact process), mesoprocesses and device level. (b) Simulated energy band gap (E_g), intrinsic Fermi levels (E_i), and electric field (e) distribution. (c) Impact ionization count versus position for the standard p-i-n structure. (d) Total electron count. (e) Simulated energy band gap (E_g), intrinsic Fermi levels (E_i), and electric field (e) distribution. (f) Impact ionization count versus position for the ML structure. (g) Total electron count. (h) Simulated energy band gap (E_g), intrinsic Fermi levels (E_i), and electric field (e) distribution. (i) Impact ionization count versus position for the AML structure. (j) Comparison of simulated BBT current versus reverse bias. (k) Comparison of multiplication gain and (l) *gain fluctuation* versus reverse bias for all three structures.

acterizes the efficiency of the electric field in driving the avalanche.

Critically, these parameters are not independent. Our mesoscopic analysis reveals a profound physical coupling exists between them, rooted in the underlying microscopic scattering mechanisms. For instance, as ℓ increases (corresponding to a weaker internal field), the carrier's flight time lengthens, increasing the probability of POP scattering [16]. This microscopic scattering deflects the electron's trajectory, thereby directly increasing the mesoscopic spatial uncertainty, σ. This intrinsic temporal–spatial coupling means APD optimization is a constrained optimization problem in a 2-D space, not a simple 1-D minimization.

Leveraging the (σ, ℓ) framework, we analyze the evolutionary path of device structures. The central goal of this analysis is to identify a physical structure that can actively engineer the mesoscopic state, specifically to transform the avalanche process from a random, spatially diffused phenomenon (high σ) into a deterministic, localized one (low σ). This leads to the concept of the ML—a class of structures that engineer the band profile [see Fig. 3(e)] at the mesoscopic scale using periodic lattice-like heterojunctions to actively regulate carrier dynam-

Authorized licensed use limited to: Shanghai Institute of Technical Physics CAS. Downloaded on April 01,2026 at 02:47:06 UTC from IEEE Xplore. Restrictions apply.

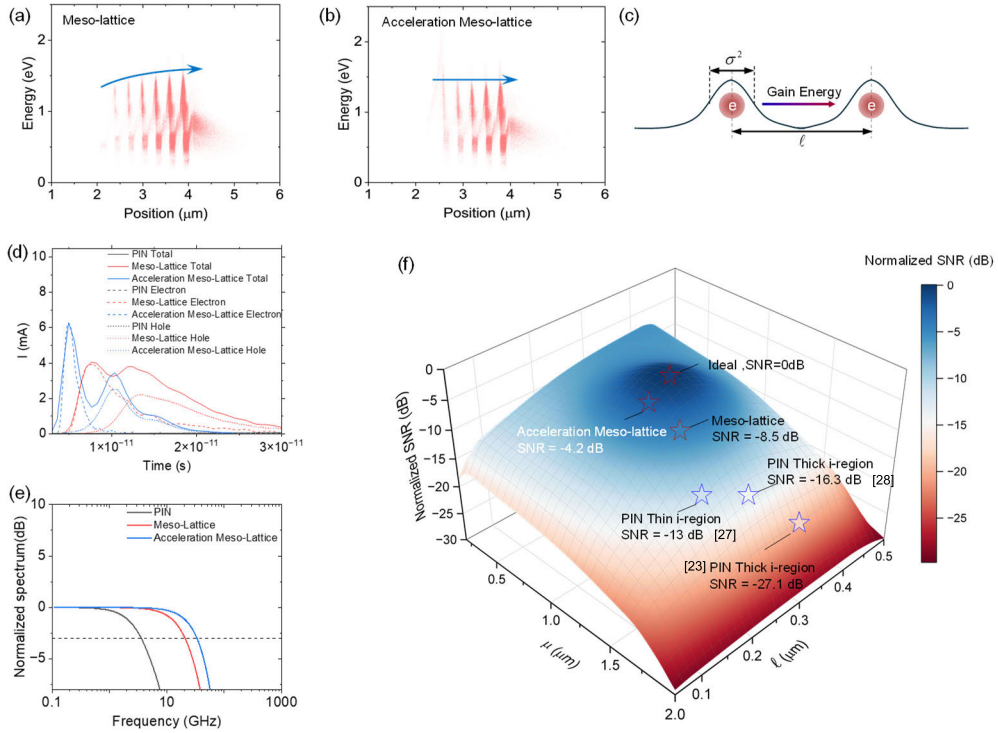


Fig. 4. Analysis of spatial, temporal, and noise characteristics for the simulated device models. Comparison of electron energy (eV) as a function of position for (a) ML and (b) AML models. (c) Definition of key performance metrics: degree of spatial separation (σ) and degree of temporal sequence maintenance (ℓ). (d) Simulated transient response, plotting electron current and total current (I) versus time for the p-i-n, ML, and AML models. (e) Comparison of the normalized frequency spectrum (dB) for the three models. (f) Normalized SNR analysis, plotting SNR (dB) as a function of spatial separation (σ) and temporal maintenance (ℓ). The plot compares the AML (SNR ≈ −4.2 dB) and ML (SNR ≈ −8.5 dB) models against an ideal baseline and standard p-i-n structures (thick and thin i-region) [23], [27], [28].

TABLE I
STRUCTURAL PARAMETERS OF THE AML

Layer name	Cd mole fraction	Doping(cm^{-3})	Thickness (μm)
p-layer	0.3	7×10^{18}	2
Acceleration	0.355	1×10^{17}	0.5
Meso-Lattice	0.17~0.36	1×10^{14}~8×10^{18}	1.5

ics. Our first attempt, the ML structure, sought to separate acceleration and multiplication using periodic heterojunctions. However, our analysis revealed an intrinsic limitation. As shown in the simulation results [see Fig. 3(f)], the impact ionization count for this structure, while more ordered than the p-i-n [see Fig. 3(c)], still exhibited a distinct multipeak, diffuse morphology, with ionization events occurring probabilistically after different steps. This conclusively demonstrates that the process remains highly stochastic. In the (σ, ℓ) space, this structure remains in the high-σ domain, its probabilistic energy injection mechanism [visualized in the trajectory analysis of Fig. 4(a)] failing to suppress the BBT-inducing fluctuations.

Based on this understanding, we proposed the AML structure, which features an engineered band gap, Fermi level, and electric field distribution [see Fig. 3(h)]. Table I details AML parameters: Cd fraction, doping, and thickness. Its key innovation is a wide, independent initial acceleration region preceding the main multiplication region. This zone's function is to provide a one-time, deterministic energy calibration, ensuring all the electrons are precisely calibrated near the ionization threshold E_{th} before entering the subsequent low-field multiplication region. This is validated by two key results. First, the electron energy trajectories [see Fig. 4(b)] show a clear shift from the incremental, multistep energy gain of the ML [see Fig. 4(a)] to a deterministic, single-step calibration in the AML. Second, the spatial distribution of the impact ionization count [see Fig. 3(i)] transforms from the diffuse distributions of the p-i-n and ML into a highly localized sharp peak. This demonstrates that the AML achieves active positioning in the (σ, ℓ) space, realizing both an extremely small σ (a deterministic event) and an optimized ℓ (an efficient, low-noise path). This pronounced shift in the mesoscopic state is directly quantified by the macroscopic performance comparison in Fig. 3(j)–(l). The AML (blue line) not only achieves comparable multiplication gain [see Fig. 3(k)] and the lowest gain fluctuation [see Fig. 3(l)] but also reduces the BBT current by over 4 orders of magnitude compared with the p-i-n structure [see Fig. 3(j)]. In the time domain, Fig. 4(d) illustrates the AML model's distinctively faster transient response. This superior speed is reflected in Fig. 4(e), which exhibits a significantly extended 3-dB bandwidth compared with the other structures. This initial analysis suggests a simple design

Authorized licensed use limited to: Shanghai Institute of Technical Physics CAS. Downloaded on April 01,2026 at 02:47:06 UTC from IEEE Xplore. Restrictions apply.

goal: minimizing σ appears to be the primary objective for high performance.

However, our physical analysis reveals this $\sigma \to 0$ conclusion is an oversimplification. APD performance is not a 1-D minimization problem but is dictated by a multinoise competition in the full 2-D (σ, ℓ) parameter space, as plotted in the normalized SNR (dB) analysis in Fig. 4(f). The optimal SNR is not found at the absolute minimum $\sigma = 0$, as another noise mechanisms emerge as a physical limit. The device noise, N_{total}, is a complex function of $N_{total} = f(N_{Auger}, N_{BBT}, N_{POP}, N_{Excess})$, where each component is strongly coupled to (σ, ℓ) [29], [30]. We identified four primary competing mechanisms. At the extremely small σ limit, two mechanisms dominate: Auger noise (N_{Auger}), which surges as high carrier compression increases recombination probability, and directionality-induced BBT (N_{BBT}), which is enhanced by the highly coherent (low σ) electron trajectories. Together, these set a physical lower limit for σ. Conversely, at the large σ limit, two different mechanisms become dominant: fluctuation-induced BBT (N_{BBT}), the original problem in the p-i-n, triggered by high spatial randomness (stochasticity), and excess noise (N_{Excess}), as the intrinsic gain fluctuation F increases when impact becomes spatially diffuse (large σ). Finally, POP scattering acts as the crucial coupling term linking ℓ and σ. As ℓ increases (weaker field), POP scattering increases, which in turn increases σ, worsening the noise. This confirms that σ and ℓ cannot be optimized independently and sets a physical upper limit for ℓ.

To systematically analyze this multivariate competition, we constructed a normalized SNR (dB) contour plot shown in Fig. 4(f), governed by the relation $SNR \propto 1/N_{total}(\sigma, \ell)$. This analysis adheres to two key constraints: all the comparisons are performed at a fixed gain ($M = 100$), and the coordinates of other literature structures [labeled as p-i-n thick/thin i-region in Fig. 4(f)] are plotted for comparison. This SNR gradient map, $\nabla SNR(\sigma, \ell)$, reveals the complete physical optimization path. The partial derivative $\partial SNR/\partial\sigma$ is initially positive, as increasing σ from the low-σ limit effectively suppresses the dominant N_{Auger} and N_{BBT}. After peaking at σ_{opt}, $\partial SNR/\partial\sigma$ becomes negative, as N_{Excess} and fluctuation-induced N_{BBT} become dominant. Similarly, the partial derivative $\partial SNR/\partial\ell$ is first positive as the field optimizes from overstrong (inefficient impact) to ℓ_{opt}, and then becomes negative as the field becomes too weak (gain-starved and POP-dominated). This map visually proves that while conventional structures are trapped on the slopes of the suboptimal, high-σ region, our AML is actively engineered to be positioned near the summit (σ_{opt}, ℓ_{opt}).

IV. Conclusion

In conclusion, this work's primary contribution is the analysis of single-carrier avalanche mesoscopic behavior, an investigation made possible by our micro–mesoscopic simulation framework. Our analysis systematically quantifies that APD performance limits are dictated by a complex multinoise competition (Auger, BBT, POP, excess) within the full 2-D (σ, ℓ) mesoscopic parameter space. The resulting SNR landscape reveals why conventional structures (p-i-n), which suffers from high randomness (large σ) and high BBT current, are trapped in suboptimal domains. More importantly, this analysis provides the physical pathway to a solution. The AML, designed by leveraging this analysis to achieve an optimal (σ, ℓ) coordinate, serves as validation. By actively positioning the device near this optimal point, the structure effectively eliminates the physical conditions for BBT fluctuations, reducing dark current by 3–4 orders of magnitude and achieving a dramatic SNR enhancement. This work, therefore, validates the mesoscopic dynamics regulation paradigm and establishes that the analysis and engineering of the mesoscopic state provide a new physical pathway to transcend fundamental device limits. Universality extends to InSb and BP, where material properties tune specific coupling coefficients.

References

[1] P. Martyniuk et al., "Infrared avalanche photodiodes from bulk to 2D materials," *Light, Sci. Appl.*, vol. 12, no. 1, pp. 212–238, Aug. 2023, doi: 10.1038/s41377-023-01259-3.

[2] H. Jiao et al., "HgCdTe/black phosphorus van der Waals heterojunction for high-performance polarization-sensitive midwave infrared photodetector," *Sci. Adv.*, vol. 8, no. 19, May 2022, Art. no. eabn1811, doi: 10.1126/sciadv.abn1811.

[3] K. Murzyn et al., "Breaking Abbe's diffraction limit with harmonic deactivation microscopy," *Sci. Adv.*, vol. 10, no. 46, pp. 3056–3064, Nov. 2024, doi: 10.1126/sciadv.adp3056.

[4] X. Ding et al., "Detection of stellar light from quasar host galaxies at redshifts above 6," *Nature*, vol. 621, no. 7977, pp. 51–55, Sep. 2023, doi: 10.1038/s41586-023-06345-5.

[5] J. Wei, C. Xu, B. Dong, C.-W. Qiu, and C. Lee, "Mid-infrared semimetal polarization detectors with configurable polarity transition," *Nature Photon.*, vol. 15, no. 8, pp. 614–621, Aug. 2021, doi: 10.1038/s41566-021-00819-6.

[6] K. Deng et al., "All-silicon broadband infrared photodetectors with in-plane photon trapping structures," *Adv. Mater.*, vol. 37, no. 17, Apr. 2025, Art. no. 2419382, doi: 10.1002/adma.202419382.

[7] W. D. Hu et al., "Analysis of temperature dependence of dark current mechanisms for long-wavelength HgCdTe photovoltaic infrared detectors," *J. Appl. Phys.*, vol. 105, no. 10, May 2009, Art. no. 104502, doi: 10.1063/1.3130163.

[8] K. Deng et al., "High transmission efficiency long-wave infrared multispectral modulation array based on nanogap engineering," *Infr. Phys. Technol.*, vol. 142, pp. 105559–105566, Nov. 2024, doi: 10.1016/j.infrared.2024.105559.

[9] W.-C. Qiu et al., "Dark current transport and avalanche mechanism in HgCdTe electron-avalanche photodiodes," *IEEE Trans. Electron Devices*, vol. 62, no. 6, pp. 1926–1931, Jun. 2015, doi: 10.1109/TED.2015.2417193.

[10] R. J. McIntyre, "Multiplication noise in uniform avalanche diodes," *IEEE Trans. Electron Devices*, vol. ED-13, no. 1, pp. 164–168, Jan. 1966, doi: 10.1109/T-ED.1966.15651.

[11] R. J. McIntyre, "A new look at impact ionization—Part I: A theory of gain, noise, breakdown probability, and frequency response," *IEEE Trans. Electron Devices*, vol. 46, no. 8, pp. 1623–1631, Aug. 1999, doi: 10.1109/16.777150.

[12] M. A. Kinch, J. D. Beck, C.-F. Wan, F. Ma, and J. Campbell, "HgCdTe electron avalanche photodiodes," *J. Electron. Mater.*, vol. 33, no. 6, pp. 630–639, Jun. 2004, doi: 10.1007/s11664-004-0058-1.

[13] F. Bertazzi, M. Moresco, M. Penna, M. Goano, and E. Bellotti, "Full-band Monte Carlo simulation of HgCdTe APDs," *J. Electron. Mater.*, vol. 39, no. 7, pp. 912–917, Jul. 2010, doi: 10.1007/s11664-010-1198-0.

[14] I. Prigozhin, M. Zhu, and E. Bellotti, "Numerical modeling of graded bandgap long wavelength infrared HgCdTe avalanche photodiodes," *IEEE Trans. Electron Devices*, vol. 69, no. 7, pp. 3791–3797, Jul. 2022, doi: 10.1109/TED.2022.3177701.

[15] R. Xie et al., "Spatial description theory of narrow-band single-carrier avalanche photodetectors," *Opt. Exp.*, vol. 29, no. 11, pp. 16432–16447, May 2021, doi: 10.1364/oe.418110.

[16] R. Xie et al., "Role of neutral impurities and non-parabolic dispersive electrons in HgCdTe avalanche photodiodes," *Opt. Lett.*, vol. 50, no. 8, pp. 2723–2727, Apr. 2025, doi: 10.1364/ol.554273.

Authorized licensed use limited to: Shanghai Institute of Technical Physics CAS. Downloaded on April 01,2026 at 02:47:06 UTC from IEEE Xplore. Restrictions apply.

[17] J. W. Harrison and J. R. Hauser, "Alloy scattering in ternary III–V compounds," *Phys. Rev. B, Condens. Matter*, vol. 13, no. 12, pp. 5347–5350, Jun. 1976, doi: 10.1103/physrevb.13.5347.

[18] S. Mazoyer, J. P. Hugonin, and P. Lalanne, "Disorder-induced multiple scattering in photonic-crystal waveguides," *Phys. Rev. Lett.*, vol. 103, no. 6, pp. 63903–63907, Aug. 2009, doi: 10.1103/physrevlett.103.063903.

[19] A. Go"ıcoechea et al., "Reflection measurement of the scattering mean free path at the onset of multiple scattering," *Phys. Rev. Lett.*, vol. 133, no. 17, pp. 176301–176305, Oct. 2024, doi: 10.1103/physrevlett.133.176301.

[20] B. Nachman, D. Provasoli, W. A. de Jong, and C. W. Bauer, "Quantum algorithm for high energy physics simulations," *Phys. Rev. Lett.*, vol. 126, no. 6, p. 62001, Feb. 2021, doi: 10.1103/physrevlett.126.062001.

[21] S. D. March, A. H. Jones, J. C. Campbell, and S. R. Bank, "Multistep staircase avalanche photodiodes with extremely low noise and deterministic amplification," *Nature Photon.*, vol. 15, no. 6, pp. 468–474, Jun. 2021, doi: 10.1038/s41566-021-00814-x.

[22] S. Derelle, S. Bernhardt, R. Hardar, J. Primot, J. Deschamps, and J. Rothman, "A Monte Carlo study of *Hg_0.7Cd_0.3Te* e-APD," *IEEE Trans. Electron Devices*, vol. 56, no. 4, pp. 569–577, Apr. 2009, doi: 10.1109/TED.2009.2012526.

[23] S. Derelle et al., "Experimental performance and Monte Carlo modeling of long wavelength infrared mercury cadmium telluride avalanche photodiodes," *J. Electron. Mater.*, vol. 38, no. 8, pp. 1628–1636, Aug. 2009, doi: 10.1007/s11664-009-0827-y.

[24] S. K. Singh, V. Gopal, R. K. Bhan, and V. Kumar, "An analysis of the dynamic resistance variation as a function of reverse bias voltage in a HgCdTe diode," *Semicond. Sci. Technol.*, vol. 15, no. 7, pp. 752–757, Jul. 2000, doi: 10.1088/0268-1242/15/7/315.

[25] T. Nguyen, C. A. Musca, J. M. Dell, J. Antoszewski, and L. Faraone, "Dark currents in long wavelength infrared HgCdTe gated photodiodes," *J. Electron. Mater.*, vol. 33, no. 6, pp. 621–629, Jun. 2004, doi: 10.1007/s11664-004-0057-2.

[26] P. D. Anderson et al., "Recent advancements in HgCdTe APDs for space applications," *J. Electron. Mater.*, vol. 51, no. 12, pp. 6803–6814, Dec. 2022, doi: 10.1007/s11664-022-09873-4.

[27] J. Rothman et al., "Meso-photonic detection with HgCdTe APDs at high count rates," *J. Electron. Mater.*, vol. 49, no. 11, pp. 6881–6892, Nov. 2020, doi: 10.1007/s11664-020-08461-8.

[28] A. Kerlain et al., "Performance of mid-wave infrared HgCdTe e-Avalanche photodiodes," *J. Electron. Mater.*, vol. 41, no. 10, pp. 2943–2948, Oct. 2012, doi: 10.1007/s11664-012-2087-5.

[29] Q. Li, J. He, W. Hu, L. Chen, X. Chen, and W. Lu, "Influencing sources for dark current transport and avalanche mechanisms in planar and mesa HgCdTe p-i-n electron-avalanche photodiodes," *IEEE Trans. Electron Devices*, vol. 65, no. 2, pp. 572–576, Feb. 2018, doi: 10.1109/TED.2017.2783352.

[30] F. Ma, S. Wang, and J. C. Campbell, "Shot noise suppression in avalanche photodiodes," *Phys. Rev. Lett.*, vol. 95, no. 17, pp. 176604–176608, Oct. 2005, doi: 10.1103/physrevlett.95.176604.

Authorized licensed use limited to: Shanghai Institute of Technical Physics CAS. Downloaded on April 01,2026 at 02:47:06 UTC from IEEE Xplore. Restrictions apply.